Sahu et al. *NPG Asia Materials* (2023) 15:49
https://doi.org/10.1038/s41427-023-00497-6

NPG Asia Materials

ARTICLE Open Access

Free-standing 2D gallium nitride for electronic, excitonic, spintronic, piezoelectric, thermoplastic, and 6G wireless communication applications

Tumesh Kumar Sahu[1,2], Saroj Pratap Sahu[3,4], K. P. S. S. Hembram[5], Jae-Kap Lee[5], Vasudevanpillai Biju[6] and Prashant Kumar[1,7]

Abstract
Two-dimensional gallium nitride (2D GaN) with a large direct bandgap of ~5.3 eV, a high melting temperature of ~2500 °C, and a large Young's modulus ~20 GPa developed for miniaturized interactive electronic gadgets can function at high thermal and mechanical loading conditions. Having various electronic, optoelectronic, spintronic, energy storage devices and sensors in perspective and the robust nature of 2D GaN, it is highly imperative to explore new pathways for its synthesis. Moreover, free-standing sheets will be desirable for large-area applications. We report our discovery of the synthesis of free-standing 2D GaN atomic sheets employing sonochemical exfoliation and the modified Hummers method. Exfoliated 2D GaN atomic sheets exhibit hexagonal and striped phases with microscale lateral dimensions and excellent chemical phase purity, confirmed by Raman and X-ray photoelectron spectroscopy. 2D GaN is highly stable, as confirmed by TGA measurements. While photodiode, FET, spintronics, and SERS-based molecular sensing, IRS element in 6G wireless communication applications of 2D GaN have been demonstrated, its nanocomposite with PVDF exhibits an excellent thermoplastic and piezoelectric behavior.

Introduction

Xenes, MXenes, and boron nitride constitute a novel class of 2D materials[1–7]. Recently, there has been a tremendous surge in exploring these materials and manipulating their properties towards next-generation electronic materials[8–15]. While 2D materials are apt for electronic gadgets and sensors due to high mobility, next-generation power electronics need 2D materials working under extreme thermal conditions. High melting points and large bandgap 2D materials are continuously being sought-after. GaN, a member of group-III nitrides, is a thermally robust (T_m ~ 2500 °C) and a direct bandgap (ca. 5.3 eV) semiconductor technologically relevant for such applications. Also, GaN and its derivatives are promising for LEDs, lasers, portable batteries, and high-power radio frequencies (RF) amplifiers[16–21]. The growth of stoichiometric GaN atomic layers is essential for realizing such applications. Also, 2D GaN is a dream material for atomically thin barriers in tunnel junctions, single-photon emitters, 2D sensors, thermoplastics, polarization-driven topological insulators, and batteries[22–27]. Wurtzite GaN is predicted to reconstruct into a 2D hexagonal graphitic structure showing thickness-dependent bandgap (E_g) engineering via quantum confinement.

Compared with its bulk counterpart, the wide bandgap of 2D GaN structures enable electronic components to hold their durability even at a higher voltage in power devices and forms quantum wells emitting photons in the deep-UV range. Given theoretical predictions of such unique excitonic properties to 2D GaN, it is timely to develop GaN-based 2D materials and characterize their structures and properties. 2D GaN is experimentally

Correspondence: Vasudevanpillai Biju (biju@es.hokudai.ac.jp) or
Prashant Kumar (Prashant.Kumar@newcastle.edu.au)
[1]Department of Physics, Indian Institute of Technology Patna, Bihta Campus, Patna 801103, India
[2]Department of Physics, Shri Ramdeobaba College of Engineering and Management Nagpur, Nagpur 440013, India
Full list of author information is available at the end of the article

© The Author(s) 2023

Open Access This article is licensed under a Creative Commons Attribution 4.0 International License, which permits use, sharing, adaptation, distribution and reproduction in any medium or format, as long as you give appropriate credit to the original author(s) and the source, provide a link to the Creative Commons license, and indicate if changes were made. The images or other third party material in this article are included in the article's Creative Commons license, unless indicated otherwise in a credit line to the material. If material is not included in the article's Creative Commons license and your intended use is not permitted by statutory regulation or exceeds the permitted use, you will need to obtain permission directly from the copyright holder. To view a copy of this license, visit http://creativecommons.org/licenses/by/4.0/.

realized by graphene encapsulation, graphene oxide templating, or by chemical transformation of gallium sulfide[26–28]. Despite graphene encapsulation or templating under extreme reaction conditions, the product formed behaves like a hybrid between GaN and Graphene. It is, therefore, still challenging to develop chemically pure 2D GaN without any defects/vacancies or traces of sulfur. Free-standing 2D GaN will significantly advance its long-awaited roles in future electronics, sensors, and the energy sector.

We have synthesized free-standing 2D GaN by sonochemical and modified Hummer's methods and characterized the product's crystal structures and chemical purity using microscopic and spectroscopic techniques. While its magnetism is explored, it has been used as an anchor in surface-enhanced Raman spectroscopy (SERS)-based molecular sensing. Also, we fabricated a photodiode using 2D GaN hetero-layered with graphene and explored the FET applications. Further, we demonstrate the mechanical, piezoelectric, and fire-retardant properties of GaN–poly (vinylidene fluoride) (PVDF) nanocomposites.

Results and discussion

Sonochemical synthesis of 2D GaN (or GNP)

2D GaN sheets were obtained by sonochemical exfoliation in various solvents like acetone, isopropyl alcohol (IPA), deionized (DI) water, *N, N*-dimethyl formamide (DMF), and toluene (see scheme in Fig. 1a and a solution containing exfoliated 2D GaN (i.e. GNP) sheets in Fig. 1b). Among solvents, exfoliation was excellent with a large sheet size in IPA, evident from the dispersion quality after 24 h in (Fig. S1 and further details in the supporting information). Thus, detailed experiments were carried out for samples synthesized in IPA. When examined with high-resolution TEM, we were surprised to see free-standing atomic sheets formed in IPA. We zoomed in and scanned the TEM samples and observed the minute structural details of the as-synthesized GNP samples. For example, three distinct structures (namely, hexagonal, linear, and curvilinear) were observed (Fig. 1c). Figure 1c1 shows that Ga and N make hexagonal patterns with Ga–Ga distances at 2.4 Å, N–N at 2.9 Å and Ga–N at 1.9 Å. Incidentally, the inset FFT exhibits a hexagonal pattern. Figure 1c2 shows a linear structure in another area, with the distances between the atoms equal to the Ga–Ga distance in Fig. 1c1. Also, the TEM images show highly strained exfoliated sheets.

When a TEM image was analyzed in detail, as shown in the zoomed-in view Fig. 1d1, a highly ridge-like structure was observed, where one atomic array is up and the other down in a periodic manner. Such an intertwined ridge-like structure suggests the unstable 2D GaN buckled structure predicted by theoretical calculations. Exhilarated with such a finding, we measured the atomic line profile in two directions: along the ridge and across the ridge. Along the ridge, the atomic distance was ca. 2.8 Å, and across the ridge, it was ca. 3.1 Å. Such a finding suggests that the nuclear distance is increased from 2.4 to 2.8 Å for the Ga–N bond. However, Ga and N atoms were ca. 1.4 Å apart in some locations, which was way closer than the usual Ga–N bond length. Atoms at such a compromised distance would be under severe localized strain or show a high-energy Eigen structure. Inset in Fig. 1d1 shows hexagonal symmetry in the FFT pattern having a central line. The high packing density of atoms would result in a tremendously high localized strain in the system responsible for the curvature of the cluster itself. The hexagonal structure in free-standing sheets (Fig. 1d1 and the FFT in the inset) is surprising as an atomic size difference and a valency disparity in Ga–N would instead cause enormous strain, destabilizing the material as was earlier proposed by Balushi et al.[26]. To obtain a strain-free sample, graphene was used for encapsulation and stabilizing the Ga–N hexagonal structure. However, strain-free locations are limited, and we observed varieties of impacts strain brings to the resulting atomic structures. Ga and N atoms, being different in size and valency, interact with each other and often form –Ga–N–Ga–N– chains. As the neighboring atoms in the chain interact, inter-chain atomic interactions are reduced. Thus, the two atomic chains remain at 3.1 Å apart (Fig. 1e). The atoms in the free-standing sheets become thermodynamically stable by forming the ripple structure, as demonstrated in several 2D materials, including graphene[29,30]. However, the ripples in the present case are well aligned, a few atoms wide, extend to hundreds of nm, and are separated by ca. 2.5 nm. Conversely, graphene forms randomly oriented ripples 100 nm wide and extended up to a few microns. We have observed 2 nm wide regular ripples in the 2D GaN sheets, which is common to 2D materials for strain releasing.

AFM images show 2D GNP sheets with ca. 60 nm, lateral dimension, and ca. 0.3 nm height, suggesting monolayer layers (Fig. 1f). Raman spectrum obtained for GNP sheets is shown in Fig. 1g, which exhibits characteristic peaks at 410, 560 (E_2^H mode), and 714 (A1 LO mode) cm^{-1}. As the hexagonal phase of GaN belongs to the würtzite structure with the P63mc space group, it is expected to have six Raman modes[31,32]. When deconvoluted for the samples centrifuged at different speeds, a broad peak in the 500–620 cm^{-1} region was resolved into primarily four modes. Out of which, the behavior of E_2^H and A1 was studied. Interestingly, while the E_2^H mode is unchanged with a change in the number of layers; the A1 mode became softened (Fig. 1h). As the number of layers gradually increases, the inter-layer distance decreases, and the interlayer interaction increases, activating out-of-plane modes and deactivating in-plane vibrational modes.

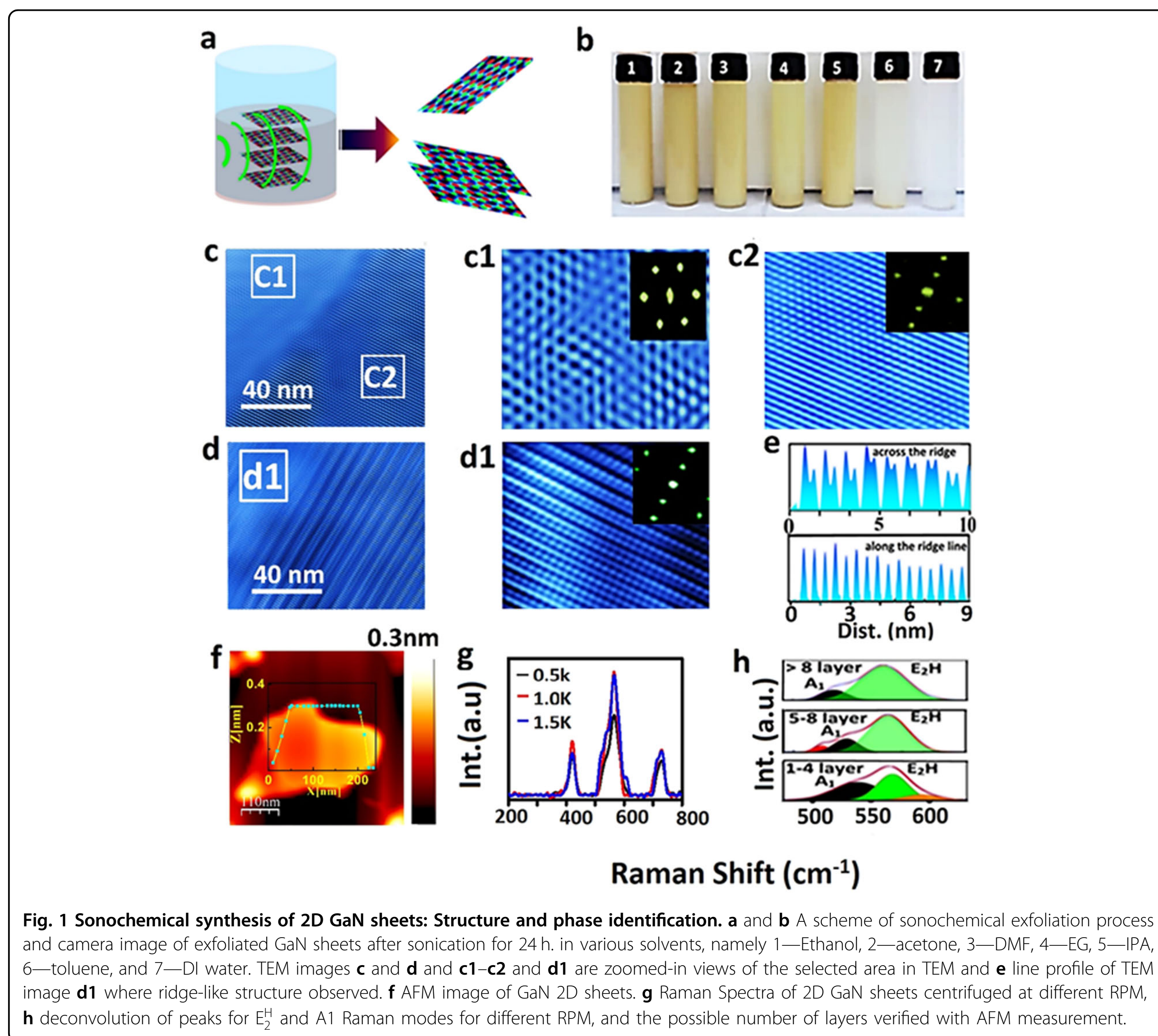

Fig. 1 Sonochemical synthesis of 2D GaN sheets: Structure and phase identification. **a** and **b** A scheme of sonochemical exfoliation process and camera image of exfoliated GaN sheets after sonication for 24 h. in various solvents, namely 1—Ethanol, 2—acetone, 3—DMF, 4—EG, 5—IPA, 6—toluene, and 7—DI water. TEM images **c** and **d** and **c1**–**c2** and **d1** are zoomed-in views of the selected area in TEM and **e** line profile of TEM image **d1** where ridge-like structure observed. **f** AFM image of GaN 2D sheets. **g** Raman Spectra of 2D GaN sheets centrifuged at different RPM, **h** deconvolution of peaks for E_2^H and A1 Raman modes for different RPM, and the possible number of layers verified with AFM measurement.

Layer-dependent peak positions, FWHM, relative peak area, and $\Delta\omega$ for E_2^H and A1 are presented in Fig. S2. Details of the layer-dependent behavior of different modes are given in the supporting information, and the behavior is similar to metal dichalcogenides[31,32]. Solvents have a significant impact on the exfoliation of 2D materials and their yield. Solvents with intercalation and swelling capabilities can separate the layers of 2D materials, aiding in exfoliation. Proper solvation and dispersion of the 2D material flakes by solvents of appropriate polarity and surface tension prevent re-aggregation, leading to higher yield. Solvent properties such as surface energy, viscosity, and volatility influence interactions, process control, and the formation of thin, defect-free flakes. Considering the environmental impact of solvents is crucial. The choice of solvent should be optimized based on the specific 2D material to achieve optimal exfoliation yield. Sonochemical exfoliation of 2D GaN was performed using acetone, DI water, and IPA solvents. Raman spectroscopy showed distinct peaks for each solvent: acetone (693, 536, 388, and 226 cm^{-1}), DI water (690, 597, 511, 418, and 262 cm^{-1}), and IPA (714, 561, 533, 410, and 310 cm^{-1}). FTIR analysis revealed characteristic vibrational signatures of GaN: 458 cm^{-1} (zone boundary phonon), 515 cm^{-1} (A1 (TO)), 514 cm^{-1} (E2 (high)), 611 cm^{-1} (SO phonon), 671 cm^{-1} (A1 (LO)), and 740 cm^{-1}. Changes were observed in FTIR spectra of DI water-synthesized GaN, including a peak shift at 951 cm^{-1} and a new peak at 1013 cm^{-1}, indicating oxy-nitride group formation and structural modifications. Solvent selection influences the Raman and FTIR spectra, highlighting its impact on GaN's chemical behavior.

These FTIR results of GaN exfoliation in DI water solvent clearly represent the interaction and strong functionalization of GaN sheets and new phase formation (Fig. S3 and further details in the supporting information). TEM was employed to critically examine the effect of solvent on morphological features of the products obtained via sonochemical exfoliation (Figs. S4–S8, details in supporting information. In our observations, we noted that the sheets exfoliated with isopropyl alcohol (IPA) exhibited larger sizes and higher exfoliation yields while maintaining the high crystallinity of the Hexagonal phase. This was confirmed by the SEAD pattern, which showed the presence of family planes such as (100), (200), (220), and (101). By calculating the d-spacing, we determined a value of 1.21 Å for the (102) plane, which demonstrated good agreement between the experimentally obtained and theoretically predicted d-spacing for the hexagonal phase of the GaN sheet more details can be found in ESI Section (4).

Having confirmed the 2D structure of sonochemically exfoliated GaN sheets, it was imperative to explore the band structure of the flat free-standing sheets. Our DFT band structure and Density of States (DOS) calculations with adequate consideration of lattice (Figs. 2a, S10–S14, and Table 1) reveal monolayer band structures and quantum confinement in GaN sheets (Fig. 2b). Lattice constants and cohesive energies of monolayer and bulk structures are compared in Table 2, and the details are in supporting information. The bandgap in 2D GaN is ca. 3 eV at Γ-point. This value is appreciable in contrast with the often-underestimated values in DFT calculations. Earlier literature also predicted the bandgap close to it[33]. We observed different band gaps for the synthesized samples centrifuged at two different speeds. While a lower speed (4k RPM) resulted in a lower bandgap (ca. 3.1 eV), and a higher speed (6k) resulted in a higher bandgap (ca. 5.6 eV) sample, which indicates a monolayer (Fig. 2c). More than one bandgap 2D sheet can arise due to the coexistence of different phases or a different number of layers in the same sample[26]. XPS measurements were carried out (Fig. 2d) to confirm the chemical phase and valency of the GNP samples, and short-range Ga 3d and N 1s peaks (Fig. 2e and f) were detected. The Ga 3d bands at 19.3 eV (–N bond) and 21.9 eV (–NO bond) were resolved upon deconvolution. Upon deconvolution of the N 1s peak, we detected stretches at 397 eV (for –N bond) and 401 eV (for –NO bond)[34–37]. A double bond would form when Ga and N are at closer distances. Otherwise, these atoms form a single bond. A 2D lattice becomes strained when formed from atoms having significant size differences, changing bond lengths, and bond angles[38,39]. In the formation process or afterward, it can reconfigure itself to other stable structures with minimal energy triggers.

Applications of GNP

Electronic property and field effect transistor (FET) behavior

We could observe a nonlinear I–V characteristic with ca. 0.2 μA at 2 V, resulting in the resistivity of 7.8×10^1 Ω cm (Fig. 2g), which is expected from a semiconducting material. The FET device was fabricated using 2D GNP as active material and back gate configuration was used for the measurements (Fig. 2h, i). One striking feature of the device is operating at high voltage without any failure, and this is useful for high-power electronics (Fig. 2j, k).

SERS application

GaN, a good dielectric, was explored as a SERS substrate for anchoring gold nanoparticles for molecular sensing applications (Fig. 2l). We observed multifold enhancement in the Raman signature of methylene blue molecules (Fig. 2m). At the concentration where there is almost no Raman signal of MB in gold NP/glass, 2D GNP as dielectric was observed to make the distinct signals well identifiable.

Modified Hummer's method synthesis of 2D GaNO and its exfoliation and reduction or chemically exfoliated 2D GaN (or GNC)

A modified Hummer's method is employed to overcome the limitations facing sonochemical exfoliation, especially scalability issues[40–42]. Formation of oxygenated GaN is imminent which requires reduction (Figs. 3a and S9). Details of synthesis, the mechanism of exfoliation, and the reduction are included in the supporting information. Typical sheet-like features are observed in TEM (Fig. 3b) With lateral dimensions 60–300 nm for two- or three-layered structures. We precisely measured the monolayer thicknesses of 2D GaN sheets using AFM and found 0.3 nm corresponding to the monolayer (Fig. 3c, d). Raman spectroscopy attests to the chemical fingerprint and the 2D nature of free-standing GaN sheets[38,43]. We detected prominent Raman peaks at 313, 370, 478, and 651 cm^{-1} Fig. 3e). The peak at 478 cm^{-1} is assigned to the GaN crystal, whereas the 651 cm^{-1} peak represents defects formed by strain in the 2D structure. Also, the peak at 370 cm^{-1} corresponds to defects. X-ray photoelectron spectroscopy (XPS) data (Fig. 3f) exhibit the signature of Ga 3d and N 1s orbitals. The band for Ga 3d is between 16 and 28 eV (Fig. 3g). We resolved it into two peaks by deconvolution, one at 19.45 eV for Ga–N–O and the other at 22.60 eV for Ga–N. The N 1s band was in the 390–500 eV range (Fig. 3h). This broadband was deconvoluted into one at 396.68 eV for Ga–N and another at 399.48 eV for Ga–N–O.

Thus, XPS results indicate the presence of N–O bonds. Even though DMF is a reducing solvent, remnant surface functionalities contribute to small amounts of oxygen.

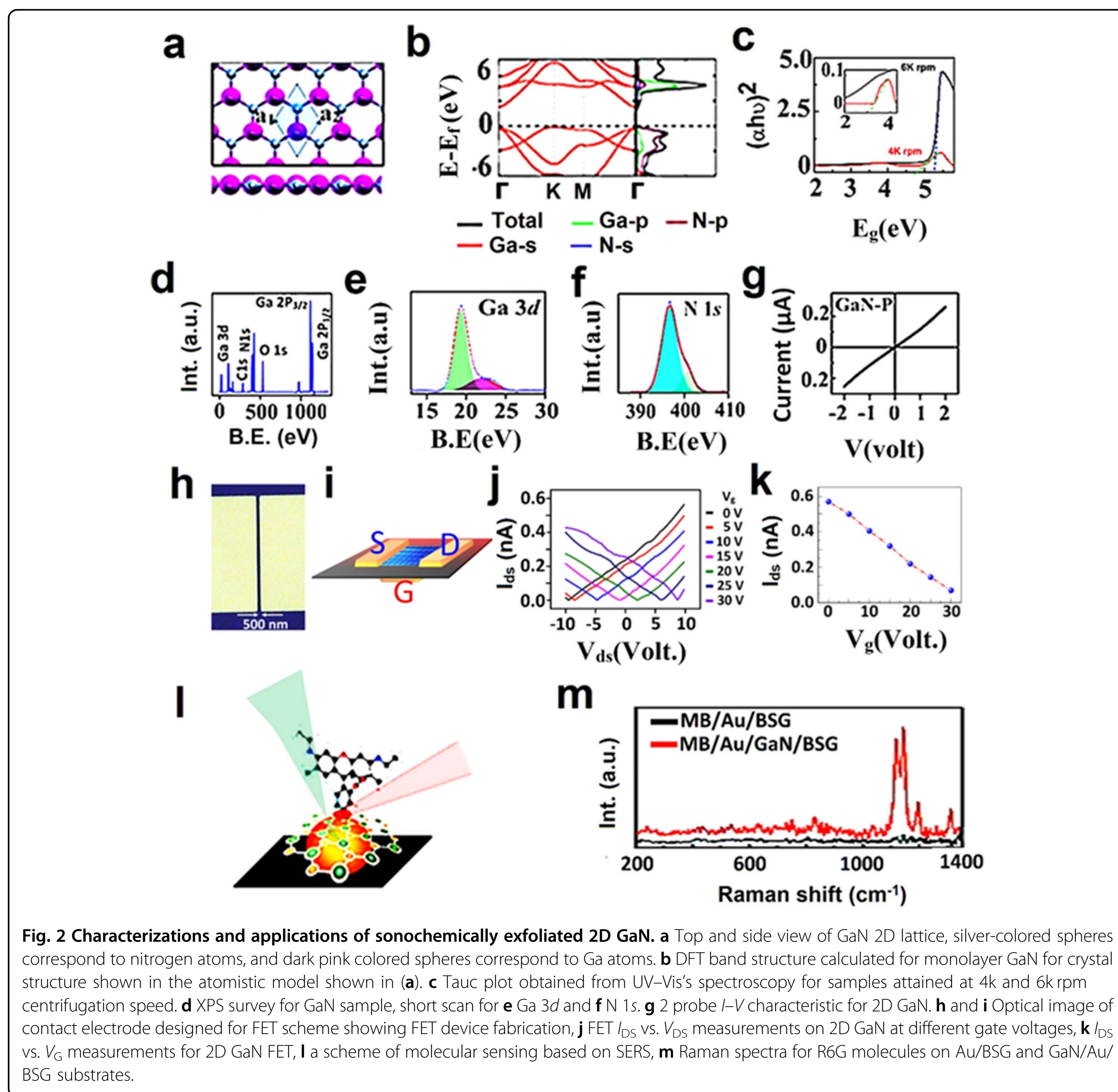

Fig. 2 Characterizations and applications of sonochemically exfoliated 2D GaN. **a** Top and side view of GaN 2D lattice, silver-colored spheres correspond to nitrogen atoms, and dark pink colored spheres correspond to Ga atoms. **b** DFT band structure calculated for monolayer GaN for crystal structure shown in the atomistic model shown in (**a**). **c** Tauc plot obtained from UV–Vis's spectroscopy for samples attained at 4k and 6k rpm centrifugation speed. **d** XPS survey for GaN sample, short scan for **e** Ga 3*d* and **f** N 1*s*. **g** 2 probe *I*–*V* characteristic for 2D GaN. **h** and **i** Optical image of contact electrode designed for FET scheme showing FET device fabrication, **j** FET I_{DS} vs. V_{DS} measurements on 2D GaN at different gate voltages, **k** I_{DS} vs. V_G measurements for 2D GaN FET, **l** a scheme of molecular sensing based on SERS, **m** Raman spectra for R6G molecules on Au/BSG and GaN/Au/BSG substrates.

The percentage of Ga–N bonds nitroxidized was 44% for a sample prepared by the modified Hummer's technique, which was 15% for the sample prepared sonochemically. These amounts were estimated by deconvoluting the N 1*s* bands. The corresponding percentages for oxide and nitroxy bonds in GaN sheets obtained by graphene encapsulation were ca. 30%. Significantly, the sonochemical technique yielded Ga–N–O functionality better than graphene encapsulation reported by Balushi et al.[26]. Higher Ga–N–O percentages in the samples synthesized by the modified Hummer's method and subsequent reduction by the solvothermal technique are within our expectations.

Atomic resolution HRTEM images reveal prominently two phases of chemically synthesized GaN (GNC), the hexagonal planar phase having strain-induced defects and the striped phase having parallel ridges (Fig. 3i and zoomed-in images in (Fig. 3i(a–d)). When we compared the areal number density, i.e., the total number of atoms per nm^2 area for the two sections, we obtained 26.25 and 45.74 nm^{-2}, respectively. In contrast, the areal number density for the sonochemically synthesized GaN (GNP) sheet was 23.51 nm^{-2}, which is very close to the hexagonal phase prepared in the modified Hummer's method. We also analyzed the SEAD pattern and discovered the existence of various families of planes: (200), (102), (002), (104), (402),

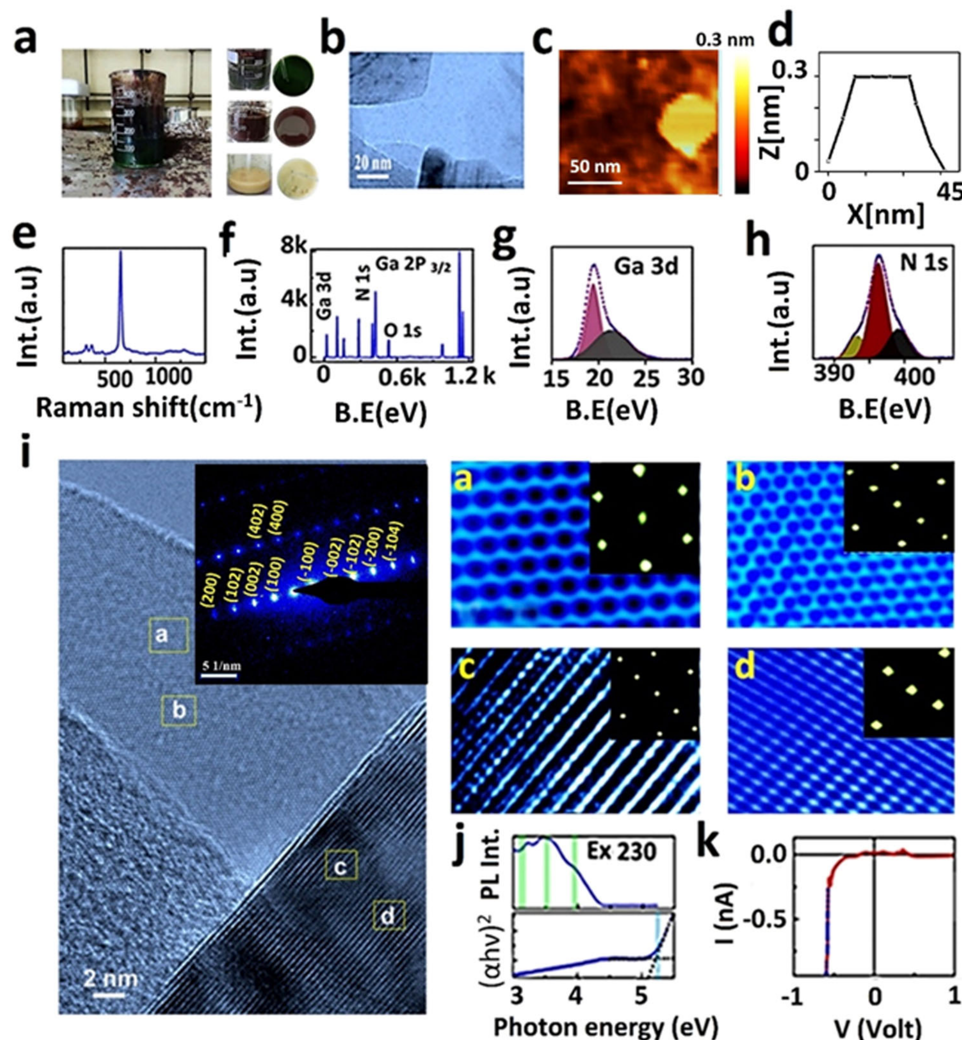

Fig. 3 Chemical (Modified Hummer's) synthesis of 2D GaN sheets: Characterizations and properties. a Camera image for chemical synthesis of 2D GaN. Camera images of the reaction mixture before heating shows green color (top image), after 24 h of heating at 65 °C show dark chocolaty color (middle image), and upon reaction, termination using H_2O_2 shows a cream color (bottom image). **b** TEM and **c** AFM images for synthesized 2D GaN. **d** AFM line profile showing monolayer 0.3 nm, **e** Raman spectrum of 2D GaN, **f** XPS survey for chemically synthesized 2D GaN, **g** short scan of Ga 3*d*, **h** short scan for N 1*s* peak. **i** HRTEM image of chemically synthesized 2D GaN sheets obtained at different locations (**a–d**). **j** UV–visible and PL spectra of 2D sheets of GaN. **k** CAFM measurement for GaN 2D sheets on FTO.

and (400). These planes strongly indicate the hexagonal structure of the synthesized 2D GaN. When we compared these findings with the XRD data, we observed the presence of similar types of family planes. The d-spacing of ~1.59 Å corresponding to the (002) plane was found to agree well with the d-spacing obtained from the XRD diffraction of the Hexagonal GaN sheet. 2D GNC sheets obtained by the modified Hummer's technique, when investigated via UV–Vis absorption spectroscopy, exhibited a bandgap of ca. 5.1 eV (Fig. 3j). When these GNC sheets were excited at 230 nm, PL peaks were ca. 2.88, 3.21, 3.58, and 4.01 eV (Fig. 3j). The high energy PL peak at 4.01 eV corresponds to the bandgap of monolayer GNC, which is shifted due to the surface functional group. The 3.58 eV peak corresponds to multilayer sheets, whereas the 2.88 and 3.21 eV peaks suggest defects such as vacancies, Stone-Wales defects, and remnant surface oxygen functionalities[44,45]. High strain in the sheets generates these defects, which segregate. High voltages were needed to attain a response in the forward bias under conducting atomic force microscopy (CAFM) when local current vs. voltage measurement (I–V) was performed for GNC atomic sheets. In contrast, the sample exhibited a sharp breakdown of ca. 0.6 V (Fig. 3k) in the reverse bias. GNC sheets in contact with a gold-coated tip behaved like a p-type material, showing Fermi-level pinning and forming a Schottky barrier.

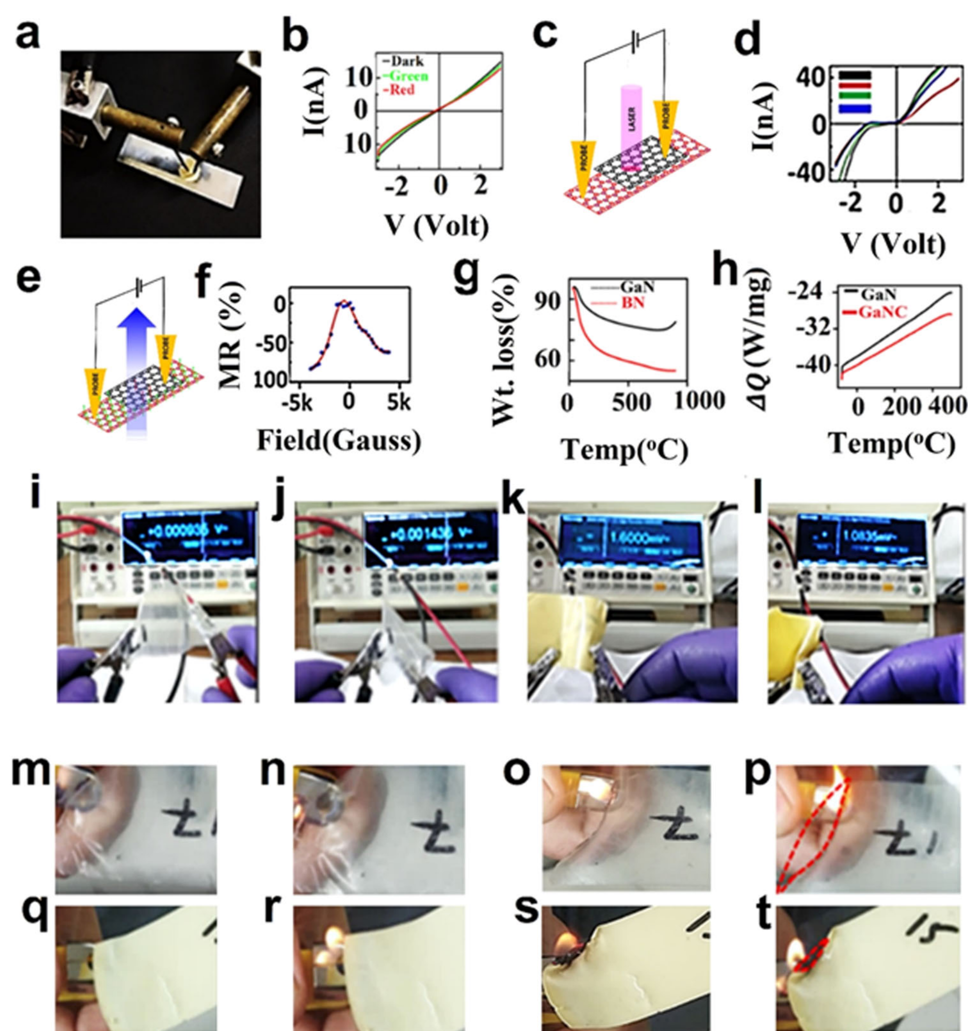

Fig. 4 Applications of chemically synthesized 2D GaN sheets. **a** Camera image of two probe setup with GNC sample, **b** photoconductivity measurements for GNC using two probe method, **c** a scheme of the device structure of GNC-Gr bilayer system for photocurrent measurements, and **d** Photocurrent response of the CVD graphene-GNC hetero-layer device with dark, red, green, and blue light source. **e** A scheme of a graphene-GNC bilayer for magnetoresistance measurements. **f** Magnetoresistance of CVD graphene–GNC bilayer system. **g** TGA data compared with BN and **h** DSC data compared with bulk GaN. Piezoelectric measurements on PVDF: **i** without strain (~0.9 mV), and **j** with compressive strain (~1.4 mV). GaN-PVDF composite piezoelectric behavior, **k** without strain (~—1.6 mV), and **l** with compressive strain (~1.03 mV). Thermoplastic behavior of PVDF, GaN-PVDF when ignited with household lighter, **m** pure PVDF at the initial stage, **n** 1 s, **o** 5 s, and **p** after 10 s. PVDF with GaN composite at different stages **q** initial, **r** 1 s, s 5 s, and **t** after 10 s.

Applications of 2D GNC

Photodiode application

Electrical characterization of individual GNC sheets obtained by the modified Hummers method followed by reduction was carried out by the 2-probe method (camera photo of measurement setup in Fig. 4a). 2D GNC sheets show tens of nA current with a signature to deviate from Ohmic behavior. The electrical response of the 2D GNC material to the light-exposed (photoconductivity) is shown in Fig. 4b. We fabricated a bilayer device with CVD graphene as the bottom layer or the substrate for GNC (schematic diagram of measurement setup in Fig. 4c). The electrical response was significant, especially with exposure to light (Fig. 4d), which exhibits photodiode behavior. A similar response was earlier reported for MoS_2/GaN[46,47], GaN/G[48], and MoS_2/Si[49,50] systems. Simulation of the designed GNC-Gr photodiode was performed to obtain the ideality factor ca. 14; see details in the ESI Section [11].

Magnetoresistance measurements

Furthermore, we examined the magnetoresistance properties of a hetero-double layer composed of GNC sheets on CVD-grown graphene sheets. We detected

negative magnetoresistance ca. 80% (the scheme in Fig. 4e and the data in Fig. 4f), which is remarkable compared to the intrinsically non-ferromagnetic nature of most monoelemental atomic sheets. Also, the TMR and DMTR behavior of GNC sheets on the CVD-grown graphene sheets was studied by simulation and found 300% TMR of the designed GNC-Gr system at room temperature for 0.6 eV spin splitting energy of graphene. We compared the obtained results with existing 2D GaN-based TMR and found the highest TMR values for our designed system; see more details in the ESI Section [10].

Piezoelectric behavior of PVDF-2D GNC nanocomposite flexible sheets

The sonochemical approach miserably fails for large-scale applications where Kg scale material production is needed. However, a modified Hummer's method has recently been employed to attain free-standing 2D materials[40–42]. Materials synthesized by this method have little remnants of surface functionalities, and therefore, adequate reduction protocol is routinely followed. In particular, the PVDF-2D GNC nanocomposite exhibits piezoelectric properties. Pure PVDF, without any strain, exhibited ~0.9 mV (Fig. 4i). When a compressive strain was applied, it demonstrated ~1.4 mV (Fig. 4j). In contrast, PVDF blended by GNC nanofiller, upon application of compressive strain, exhibited a change in voltage by ~2.68 mV (−1.6 to 1.08 mV) (Fig. 4k–l). The piezoelectric behavior will depend upon the loading % of GNC in PVDF and the applied strain value.

Thermoplastic behavior of PVDF-2D GNC nanocomposite flexible sheets

Further, we used 2D GNC as a nanofiller in the PVDF matrix and examined the mechanical (Fig. S15 and the details in supporting information), piezoelectric, and fire-retardant behavior. Most polymers that exhibit thermoplastic behavior have low glass transition temperatures (~100 to 150 °C). Enhancing thermoplastic and mechanical behaviors will help produce thermally and mechanically robust material. 2D materials have a high Young's modulus, e.g., graphene has $E \sim 2.4$ TPa with low thermal stability up to ~600 °C, whereas 2D GaN exhibits Young's modulus ~20 GPa with high thermal stability up to 800 °C above which oxidation occurs. Blending GaN and RGO with PVDF will enhance the thermal and mechanical behaviors and would be helpful for avionics, automotive, and Flextronics. Upon ignition with a household lighter and observing the burning rate from 0 to 10 s, the estimated burnt areas for PVDF were ~3.2 cm^2 (Fig. 4m–o); for PVDF–GNC composite, it was ~0.031 (Fig. 4q–t). The burning rate was very low (~0.031 cm^2/s) for GNC–PVDF compared to ~0.45 cm^2/s for PVDF. Higher thermal stability for the GNC–PVDF system is due to the higher melting point for GaN. Thus, the GNC–PVDF nanocomposite is promising for thermoplastic applications. 2D GaN sheets, being large bandgap materials, can find several high-temperature applications. To explore and establish the thermal integrity of GNC sheets, we carried out thermogravimetric analysis (TGA), and the samples were found thermally stable up to 800 °C, above which the weight slightly increased (Fig. 4g), suggesting the replacement of some N atoms by O atoms. For better clarity, we compared the thermal performance of GNC sheets with BN sheets, one of the most thermally stable 2D materials, and surprisingly, GNC is as stable as BN up to 800 °C. The thermal behavior of GaN is further tested by Differential Scanning Calorimetric (DSC) analysis (Fig. 4h). It reveals that the thermal conductivity of 2D GNC sheets is less than the bulk GaN, which is quite natural as the sheets have defects/functionalities. This result is significant as one can fabricate a semiconductor chip using GaN sheets that are thermally stable without the need for any extra electronic cooling system.

2D GaN-assisted intelligent reflecting surface (IRS) element for 6G wireless communication

An intelligent reflecting surface (IRS) plays a pivotal role in 6G wireless communication. It acts as a reflecting surface for an incoming signal in a controlled manner from the base station and transfers it to the user with minimal loss of signals, as shown in Fig. 5a. A 2D materials-based Intelligent reflecting surface (IRS) offers high carrier mobility, reflectivity, and bandgap tunability, and it has added advantages compared to traditional IRS materials. Here we report the design of 2D material-based IRS elements, especially GaN, graphene, and its hybrid materials in 6G wireless communication, as shown in Fig. 5c. L–C–R circuits can electronically model these IRS elements (Fig. 5b). A schematic diagram of the single hexagonal atomic sheet of graphite is shown in Fig. 5d. Graphene-based IRS element design parameters [$R = 2.4 \times 10^3\ \Omega$, $L = 1.5 \times 10^{-9}$ H, $G = 2 \times 10^{-3}$, $E_g = 0.5$ eV, $C = 1.287 \times 10^{-9}$ F, $\tau = 6$ ps, $t = 0.3$ nm, $D = 90$ μm, patch width ~10 μm and frequency range (1 THz, 3 THz)] is selected based on the literature. When conductivity variation with frequency was calculated for the graphene-based IRS system, we found that it decreased exponentially with changing the frequency for different Fermi energies and found maximum for the highest Fermi energy, as shown in Fig. 5e. This behavior is attributed to the modulation of carrier concentrations and bandgap opening at the Dirac point of graphene. When THz frequency transfers from the base station to IRS, because of the superposition process between the surface plasmonic waves of the graphene-gold system and the incident THz waves from the base station, the phase and amplitude of the reflection wave change drastically, as shown in Fig. 5f. This is due to the higher patch width of the

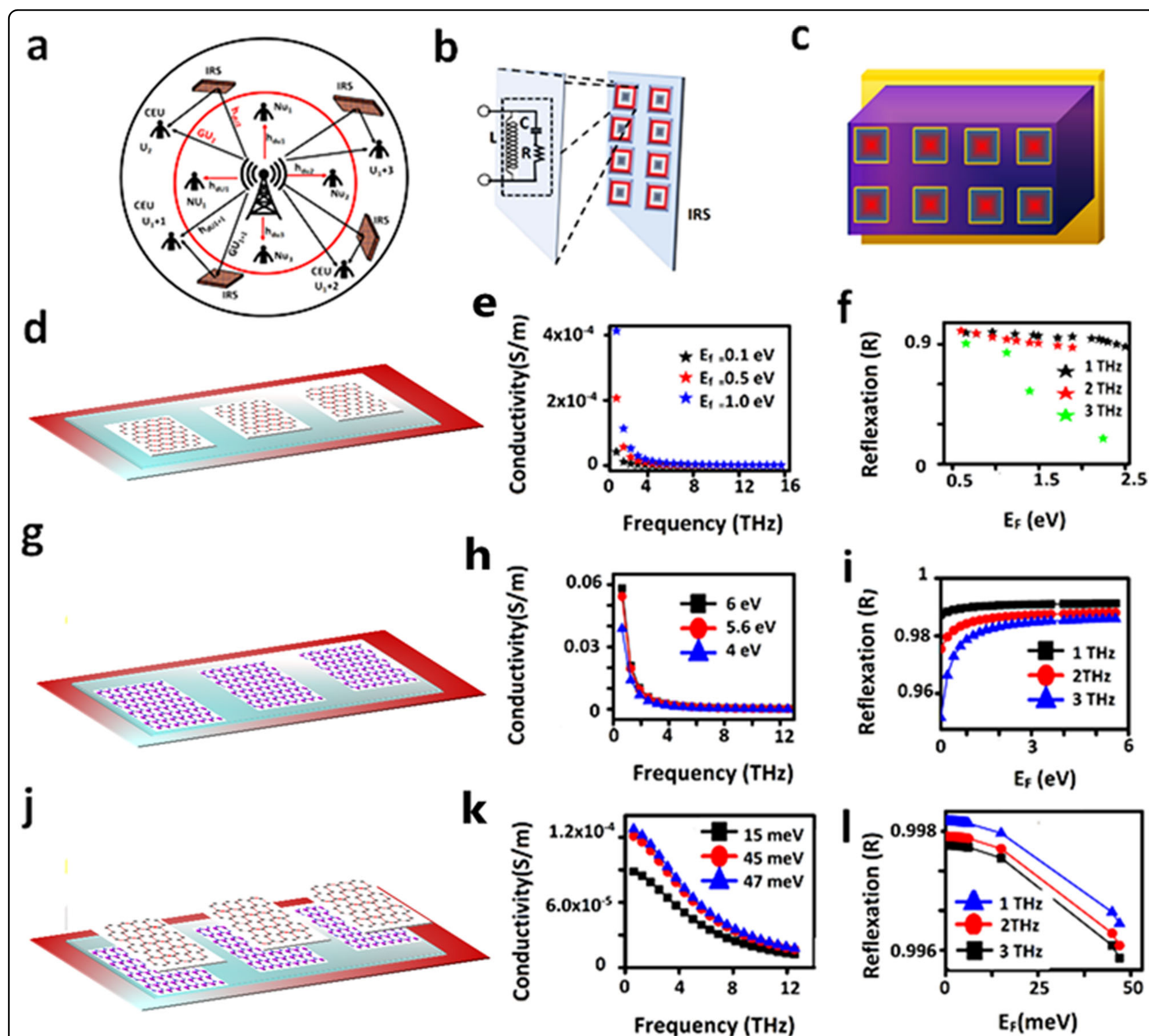

Fig. 5 6G wireless communication in 2D GaN based hybrids. a A 6G wireless communication scheme, where the signal is transmitted from the central base station to *n* number of users. Inside the red circle, users are called primary users. They directly receive the signal from the base station without fading the signal quality; outside the red circle, the users are called secondary users; they receive the signal either directly or via the IRS system. **b** An equivalent L–C–R circuit diagram of metamaterial/Au contact electrodes. **c** A scheme of various physical layers in the designed IRS surface back contact (Au), represented in yellow color, Si/SiO_2 layer in violet color and dark brown with yellow boundary illustrates the layer of 2D material/top electrode (Au). **d** A scheme of graphene layer for IRS element, **e** conductivity variation with incident frequency for graphene layer for different Fermi energy levels, and **f** reflection coefficients for graphene-based IRS elements for various frequencies. **g** A scheme of 2D GaN as the IRS element, **h** conductivity variation with incident frequency for 2D GaN layer for different Fermi energy levels, **i** reflection coefficient variations for 2D GaN-based IRS elements for different energies, **j** a scheme of 2D GaN–Gr-based hybrids as the IRS element, **k** conductivity variation for the 2D GaN–Gr layer for different frequencies and **l** reflection coefficients for 2D GaN–Gr-based IRS elements for different Fermi energies.

designed IRS element (Graphene–Au) and high operating frequency. The lower patch width leads to more confinement of the incident signal and better control over reflection with minimal loss of the THz signals. Intrinsically, graphene is a bandgap-less material and has a low carrier concentration. To overcome this issue, we applied 2D GaN as an IRS element, as shown in Fig. 5g, which is semiconducting and has a bandgap of ~ 6 eV with a marginally higher carrier concentration of ~10^{14} cm^{-2} compared to graphene. Likewise, the IRS design parameters [$R = 1.5 \times 10^6$ Ω, $L = 25 \times 10^{-9}$ H, $G = 3 \times 10^{-3}$, $E_g = [0.2\ eV, 6\ eV]$, $C = 0.1 \times 10^{-9}$ F, $\tau = 0.2$ ps, $t = 0.3$ nm, $D = 90$ μm, patch width ~10 μm, $K_0 = 20496.08$ m^{-1} and frequency range (1–3 THz)] for GaN were taken. The

conductivity variation with frequency exhibited an exponential decay behavior like graphene and found the highest conductivity ~60×10^{-3} S/m for monolayer GaN sheets, as shown in Fig. 5h. When we calculated the reflection and plotted the graph between the reflection coefficient vs. Fermi energies, we found that at lower Fermi energies, the reflection coefficient was less and became high for higher Fermi energies and saturated at the higher end, as shown in Fig. 5i. This is due to the large band gap of the 2D GaN semiconductor, which doesn't allow electron migration until it achieves a significant amount of energy for crossing the Fermi energy. Similarly, We designed a Graphene–GaN hybrid material considering its added advantages like mid-band gap opening, additional charge carrier concentration, less scattering, and higher charge carrier mobility in contrast with GaN. A scheme of the proposed IRS element GaN–Gr is shown in Fig. 5j. Similarly, the design parameters for the Gr-GaN-based IRS system were taken as $R = 2.4 \times 10^3$ Ω, $L = 3.2 \times 10^{-9}$ H, $G = 0.416 \times 10^{-3}$, $E_g = [0.2$ meV, 47 meV], $C = 0.055 \times 10^{-9}$ F, � = 0.0215 ps, $t = 0.3$ nm, $D = 90$ μm, patch width ~10 μm, $K_0 = 20496.08$ m^{-1} and the frequency range is between 1 and 3 THz. The conductivity variation with frequencies exhibited the graphene-like behavior except for the band gap parameters and found higher conductivity ~1.2×10^{-4} S/m for 47 meV bandgap, which is three orders smaller than graphene energies, as shown in Fig. 5k. This is due to the additional charge transfer from GaN to Graphene via verticle bond formation through hybridization, like the Gr-BN system[51]. When we calculated the reflection amplitude due to hybrid IRS elements and plotted the graph between the reflection vs. Fermi-energies, we found that even for the higher frequency, the variation in the reflection coefficient was more significant (Fig. 5l) than graphene, suggesting GaN to be the best-suited candidate for the IRS element.

Conclusions

We report the experimental realization of free-standing 2D GaN. It is noteworthy that while high purity 2D GaN can be achieved by the sonochemical synthesis, modified Hummer's approach is particularly scalable. While the monolayer planer hexagonal phase exhibited a bandgap of 5.3 eV, the buckled hexagonal phase exhibited 4.7 eV. CAFM measurement showed reverse breakdown with minimal voltage (~0.5 V) and p-type semiconductor behavior of 2D GaN sheets. DFT band structure calculations for 2D GaN corroborate our experimental findings. FET of 2D GaN was fabricated, and it is very robust at high voltage, which hints at high-power electronics applications. Further, 2D GaN-PVDF is excellent for next-generation thermoplastic and piezoelectric devices. The newly synthesized 2D GaN sheets are photo-responsive and potential candidates for photodetectors. The 2D GaN-RGO heterolayer exhibited excellent excitonic (photodiode), spintronic (negative MR ~ 80%) and TMR (~300%) properties. Also, 2D GaN is a promising IRS element in 6G wireless communication. Our findings on free-standing 2D GaN with novel physical properties will prompt further development of 2D GaN-based materials and their hybrids for future-generation frontline excitonic, spintronic, and IRS applications.

Associated contents

Experimental methods, synthesis of 2D GaN by sonochemical method, synthesis of 2D GaN by modified Hummer's method, microscopy and spectroscopy methods, electrical and optoelectronic measurements, theoretical calculations, mechanical/piezoelectric measurements, theoretical simulation for 6G wireless communication, TMR and DMTR calculation, diodes simulation.

Acknowledgements
We acknowledge the Department of Science and Technology, Govt. of India for a Research grant under Ramanujan Fellowship (sanction no. SB/S2/RJN-205/2014). We also acknowledge the Indian Institute of Technology Patna for providing research facilities.

Author details
[1]Department of Physics, Indian Institute of Technology Patna, Bihta Campus, Patna 801103, India. [2]Department of Physics, Shri Ramdeobaba College of Engineering and Management Nagpur, Nagpur 440013, India. [3]Department of Electronics and Communication Engineering, Indian Institute of Information Technology, Nagpur 441108, India. [4]Department of Electronics and Telecommunication, Cummins College of Engineering for Women, Nagpur 441110, India. [5]Optoelectronic Materials and Devices Research Center, Korea Institute of Science and Technology (KIST), Seoul 02792, Republic of Korea. [6]Graduate School of Environmental Science and Research Institute for Electronic Science, Hokkaido University, Sapporo, Hokkaido 060-0810, Japan. [7]Global Innovative Centre for Advanced Nanomaterials, The University of Newcastle, Newcastle 2308, Australia

Author contributions
P.K. conceived the idea. T.K.S. synthesized free-standing 2D GaN synthesis and its application. T.K.S. and S.P.S. designed the IRS element for 6G wireless communication and conducted the simulation. K.P.S.S.H. carried out DFT calculations of band structures of 2D GaN under the supervision of J.-K.L. T.K.S., P.K., and V.B. analyzed the data and wrote the manuscript. P.K. supervised the project.

Conflict of interest
The authors declare no competing interests.

Publisher's note
Springer Nature remains neutral with regard to jurisdictional claims in published maps and institutional affiliations.

Supplementary information The online version contains supplementary material available at https://doi.org/10.1038/s41427-023-00497-6.

Received: 3 May 2023 Revised: 10 July 2023 Accepted: 24 July 2023.
Published online: 22 September 2023

References

1. Novoselov, K. S. et al. Electric field effect in atomically thin carbon films. *Science* **306**, 666–669 (2004).
2. Rao, C. N. R. et al. A study of the synthetic methods and properties of graphenes. *Sci. Technol. Adv. Mater.* **11**, 054502 (2010).

3. Molle, A. et al. Buckled two-dimensional Xene sheets. *Nat. Mater.* **16**, 163–169 (2017).
4. Ranjan, P. et al. Freestanding borophene and its hybrids. *Adv. Mater.* **31**, 1900353 (2019).
5. Anasori, B., Lukatskaya, M. R. & Gogotsi, Y. 2D metal carbides and nitrides (MXenes) for energy storage. *Nat. Rev. Mater.* **2**, 1–17 (2017).
6. Kumar, P. et al. Alpha lead oxide (α-PbO): a new 2D material with visible light sensitivity. *Small* **14**, 1703346 (2018).
7. Hu, Y. et al. Water flattens graphene wrinkles: laser shock wrapping of graphene onto substrate-supported crystalline plasmonic nanoparticle arrays. *Nanoscale* **7**, 19885–19893 (2015).
8. Liu, J., Kumar, P., Hu, Y., Cheng, G. J. & Irudayaraj, J. Enhanced multiphoton emission from CdTe/ZnS quantum dots decorated on single-layer graphene. *J. Phys. Chem. C* **119**, 6331–6336 (2015).
9. Kosynkin, D. V. et al. Longitudinal unzipping of carbon nanotubes to form graphene nanoribbons. *Nature* **458**, 872–876 (2009).
10. Kumar, P., Yamijala, S. S. & Pati, S. K. Optical unzipping of carbon nanotubes in liquid media. *J. Phys. Chem. C* **120**, 16985–16993 (2016).
11. Motlag, M. et al. Asymmetric 3D elastic–plastic strain-modulated electron energy structure in monolayer graphene by laser shocking. *Adv. Mater.* **31**, 1900597 (2019).
12. Rhodes, D., Chae, S. H., Ribeiro-Palau, R. & Hone, J. Disorder in van der Waals heterostructures of 2D materials. *Nat. Mater.* **18**, 541–549 (2019).
13. Kumar, P. et al. Laser shock tuning dynamic interlayer coupling in graphene—boron nitride Moiré superlattices. *Nano Lett.* **19**, 283–291 (2018).
14. Matsubara, H. et al. GaN photonic-crystal surface-emitting laser at blue-violet wavelengths. *Science* **319**, 445–447 (2008).
15. Onen, A., Kecik, D., Durgun, E. & Ciraci, S. J. P. R. B. GaN: from three- to two-dimensional single-layer crystal and its multilayer Van Der Waals solids. *Phy. Rev. B* **93**, 085431 (2016).
16. Landmann, M. et al. GaN m-plane: atomic structure, surface bands, and optical response. *Phy. Rev. B* **91**, 035302 (2015).
17. Lai, C. F. et al. Anisotropy of light extraction from GaN two-dimensional photonic crystals. *Opt. Express* **16**, 7285–7294 (2008).
18. Weib, M., Friesicke, C., Quay, R. & Ambacher, O. Integrated 2-b Riemann pump RF-DAC in GaN technology for 5G base stations. In *IEEE MTT-S International Microwave Symposium (IMS)*, 1426–1429 (2019). https://doi.org/10.1109/MWSYM.2019.8700735.
19. Acuna, J., Seidel, A. & Kallfass, I. Design and implementation of a gallium-nitride-based power module for light electro-mobility applications. In *IEEE Southern Power Electronics Conference* (SPEC), 1–6 (2017). https://doi.org/10.1109/SPEC.2017.8333625.
20. Glavin, N. R. et al. Flexible gallium nitride for high-performance, strainable radio-frequency devices. *Adv. Mater.* **29**, 1701838 (2017).
21. Berhane, A. M. et al. Bright room-temperature single-photon emission from defects in gallium nitride. *Adv. Mater.* **29**, 1605092 (2017).
22. Guo, F. et al. Nanocomposite ultraviolet photodetector based on interfacial trap-controlled charge injection. *Nat. Nanotechnol.* **7**, 798–802 (2012).
23. Imer, B. M., Speck, J. S., DenBaars, S. P. & Nakamura, S. Growth of planar non-polar {1-1 0 0} m-plane gallium nitride with metalorganic chemical vapor deposition (MOCVD). U.S. Patent No. **7**, 338,828 (2008).
24. Miao, M. S. et al. Polarization-driven topological insulator transition in a GaN/InN/GaN quantum well. *Phys. Rev. Lett.* **109**, 18680 (2012).
25. Aggarwal, N. et al. A highly responsive self-driven UV photodetector using GaN nanoflowers. *Adv. Electron. Mater.* **3**, 1700036 (2017).
26. Al Balushi, Z. Y. et al. Two-dimensional gallium nitride realized via graphene encapsulation. *Nat. Mater.* **15**, 1166–1171 (2016).
27. Sun, C. et al. Graphene-oxide-assisted synthesis of GaN nano sheets as a new anode material for lithium-ion battery. *ACS Appl. Mater. Interfaces* **9**, 26631–26636 (2017).
28. Sreedhara, M. B., Vasu, K. & Rao, C. N. R. Synthesis and characterization of few-layer nanosheets of GaN and other metal nitrides. *Z. Anorg. Allg. Chem.* **640**, 2737–2741 (2014).
29. Bao, W. et al. Controlled ripple texturing of suspended graphene and ultrathin graphite membranes. *Nat. Nanotechnol.* **4**, 562–566 (2009).
30. Deng, S. & Berry, V. Wrinkled, rippled, and crumpled graphene: an overview of formation mechanism, electronic properties, and applications. *Mater. Today* **19**, 197–212 (2016).
31. Chakraborty, B., Matte, H. S. S. R., Sood, A. K. & Rao, C. N. R. Layer-dependent resonant Raman scattering of a few-layer MoS_2. *J. Raman Spectrosc.* **44**, 92–96 (2013).
32. Ottaviano, L. et al. Mechanical exfoliation and layer number identification of MoS_2 revisited. *2D Mater.* **4**, 045013 (2017).
33. Zhang, H., Meng, F. S. & Wu, Y. B. Two single-layer porous gallium nitride nanosheets: a First Principle Study. *Solid State Commun.* **250**, 18–22 (2017).
34. Wang, Q. et al. Interface engineering of an AlNO/AlGaN/GaN MIS diode induced by PEALD alternate insertion of AlN in Al2O3. *RSC Adv.* **7**, 11745–11751 (2017).
35. Mishra, M. et al. Pit assisted oxygen chemisorption on GaN surfaces. *Phys. Chem. Chem. Phys.* **17**, 15201–15208 (2015).
36. Li, P., Xiong, T., Wang, L., Sun, S. & Chen, C. Au-assisted epitaxy of nearly strain-free GaN films on sapphire substrates. *RSC Adv.* **10**, 2096–2103 (2020).
37. Wang, S. et al. Gallium nitride crystals: novel supercapacitor electrode materials. *Adv. Mater.* **28**, 3768–3776 (2016).
38. Davydov, V. Y. et al. Phonon dispersion and Raman scattering in hexagonal GaN and AlN. *Phys. Rev. B.* **58**, 12899 (1998).
39. Siegle, H. et al. Zone-boundary phonons in hexagonal and cubic GaN. *Phys. Rev. B.* **55**, 7000 (1997).
40. Marcano, D. C. et al. Improved synthesis of graphene oxide. *ACS Nano* **4**, 4806–4814 (2010).
41. Sahu, T. K., Ranjan, P. & Kumar, P. Chemical exfoliation synthesis of boron nitride and molybdenum disulfide 2D sheets via modified Hummers' method. *Emergent Mater.* **4**, 645–654 (2021).
42. Sahu, T. K. et al. 2+ δ-Dimensional materials via atomistic Z-welding. *Adv. Sci.* **9**, 2202695 (2022).
43. Harima, H. Properties of GaN and related compounds studied by means of Raman scattering. *J. Phys. Condens. Matter* **14**, 967–993 (2002).
44. Banerjee, S. et al. Composite GaN–C–Ga (GaCN) layers with tunable refractive index. *J. Phys. Chem. C* **122**, 29567–29576 (2018).
45. Nayak, S. K., Gupta, M. & Shivaprasad, S. M. Structural, optical and electronic properties of a Mg incorporated GaN nanowall network. *RSC Adv.* **7**, 25998–26005 (2017).
46. Ruzmetov, D. et al. Vertical 2D-3D semiconductor heterostructures based on epitaxial molybdenum disulfide and gallium nitride. *ACS Nano* **10**, 3580–3588 (2016).
47. Lee, E. W. et al. Layer-transferred MoS2/GaN PN diodes. *Appl. Phys. Lett.* **107**, 103505 (2015).
48. Tongay, S. et al. Graphene/GaN Schottky diodes: stability at elevated temperatures. *J. Appl. Phys.* **99**, 102102 (2011).
49. Pradhan, S. K., Xiao, B. & Pradhan, A. K. Enhanced photo-response in p-Si/MoS_2 heterojunction-based solar cells. *Sol. Energy Mater. Sol. Cells* **144**, 117–127 (2016).
50. Tsai, M. L. et al. Monolayer MoS_2 heterojunction solar cells. *ACS Nano* **8**, 8317–8322 (2014).
51. Ma, X. et al. Intelligent reflecting surface-enhanced indoor terahertz communication systems. *Nano Commun. Netw.* **24**, 100284 (2020).